Science Advances
AAAS

advances.sciencemag.org/cgi/content/full/5/9/eaax5196/DC1

# Supplementary Materials for

## Manipulating optical nonlinearities of molecular polaritons by delocalization

Bo Xiang, Raphael F. Ribeiro, Yingmin Li, Adam D. Dunkelberger, Blake B. Simpkins, Joel Yuen-Zhou, Wei Xiong*

*Corresponding author. Email: w2xiong@ucsd.edu

Published 27 September 2019, *Sci. Adv.* **5**, eaax5196 (2019)
DOI: 10.1126/sciadv.aax5196

**This PDF file includes:**

References (*42–46*)

## Section S1. Experimental methods

## Section S1.1. Sample preparation

The $W(CO)_6$ (Sigma-Aldrich) /cavity system is prepared in an IR spectral cell (Harrick) containing two dielectric $CaF_2$ mirrors separated by a 5, 12 or 25-μm Teflon spacer and filled with $W(CO)_6$/hexane solution (concentration varies from 5 mM to 50 mM). The dielectric mirror has a ~96% reflectivity. Because the Rabi splitting (20 to 37 $cm^{-1}$) is larger than the full-width-at-half-max of both cavity (~11 $cm^{-1}$) and $W(CO)_6$ vibrational (~3 $cm^{-1}$) modes, the strong coupling criteria are satisfied.

## Section S1.2. 2D IR spectrometer

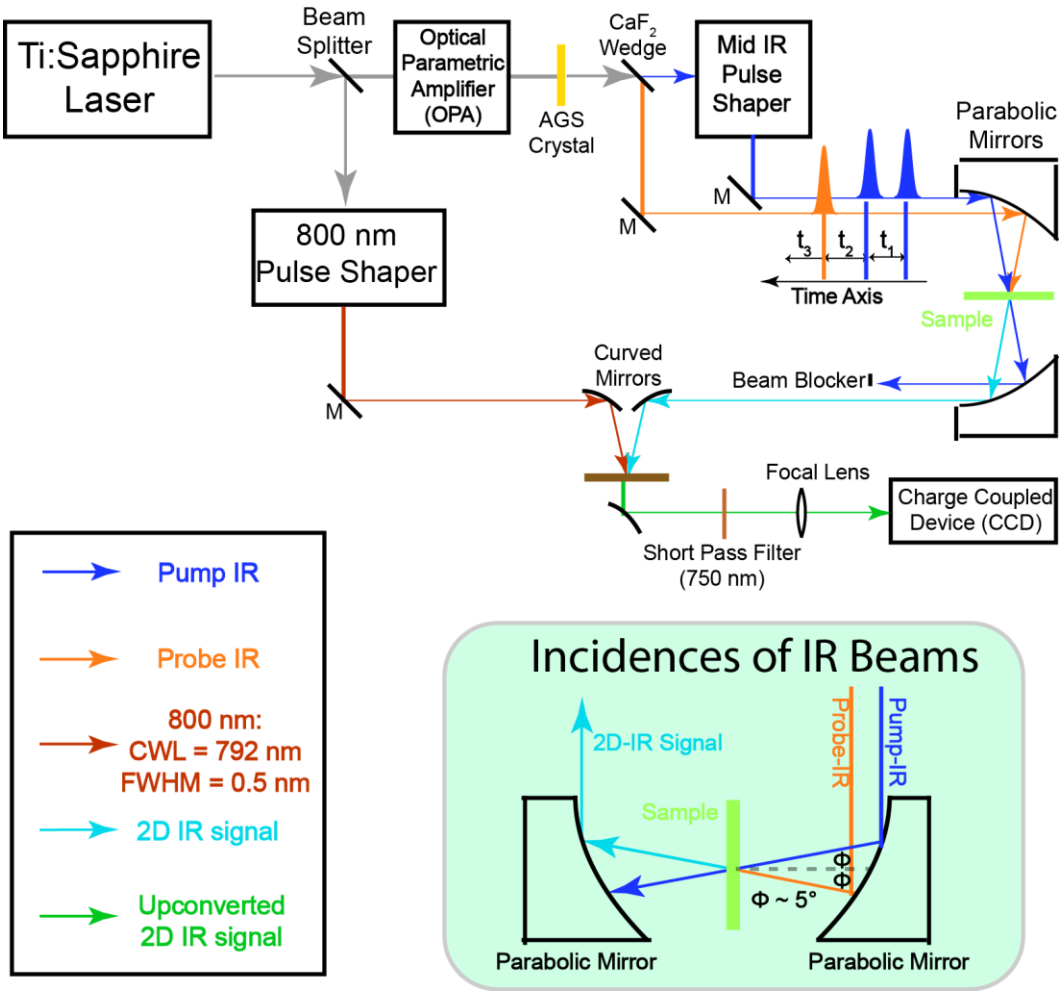


**Fig. S1. Scheme of 2D IR experimental setup**, where the inset shows the incidence of pump and probe IR beams.

Two-dimensional infrared (2D IR) spectroscopy(*14*) is applied to investigate the light-matter interaction of a $W(CO)_6$/microcavity system. The setup scheme is shown in fig. S1. 800-nm laser pulses (~35 fs, ~5 W, 1 kHz) generated by an ultrafast Ti:Sapphire regenerative amplifier (Astrella, Coherent) are sent into an optical parametric amplifier (OPA) (TOPAS, LightConversion) which outputs tunable near-IR pulses. The near-IR pulses are converted to mid-IR pulses through a difference frequency generation (DFG) process by a type II $AgGaS_2$ crystal (Eksma). After DFG, a $CaF_2$ wedge splits the mid-IR pulse into two parts: the 95% transmitted part is sent into a Ge-Acoustic Optical Modulator based mid IR pulse shaper (QuickShape, PhaseTech)(*42*) and is shaped to double pulses, which forms the pump beam arm; the 5% reflected is the probe beam. Both pump (~ 1.1 μJ) and probe (~ 0.2 μJ) are focused by a parabolic mirror (f = 10 cm) and overlap spatially at the sample. The output signal is collimated by another parabolic mirror (f = 10 cm) at a symmetric position and is upconverted to an 800-nm beam at a 5%Mg: $LiNbO_3$ crystal. The 800-nm beam that comes out of the OPA passes through an 800-nm pulse shaper which narrows its spectrum in the frequency domain (center wavelength of 791 nm and a FWHM of 0.5 nm or 9.5 $cm^{-1}$).

The pulse sequence is shown in fig. S1. Two pump pulses and a probe pulse (pulse duration of 100~150 fs) interact with samples at delayed times ($t_1$, $t_2$ and $t_3$). After the first IR pulse, a vibrational coherence is generated, which is converted into a subsequent state by the second IR pulse and is characterized by scanning $t_1$ (0 to 6000 fs with 20 fs steps) using the mid IR pulse shaper. A rotating frame at $f_0$ = 1583 $cm^{-1}$ is applied to shift the oscillation period to 80 fs and to make the scanning step meet the Nyquist frequency requirement. After waiting for $t_2$, the third IR pulse (probe) is impinged on the sample, and the resulting macroscopic polarization emits an IR signal. This IR signal is upconverted by a narrow-band 800 nm beam. The upconversion process covers the $t_3$ time delay and the 800-nm pulse duration (full width at half maximum = 0.5 nm) determines the scanning length of $t_3$. The monochromator and CCD (Andor) experimentally Fourier transform the upconverted signal, thus generating a spectrum along the $\omega_3$ axis. Numerical Fourier transform of the signal along the $t_1$ axis is required to obtain the spectrum along $\omega_1$. The resulting 2D IR spectra are plotted against $\omega_1$ and $\omega_3$. The $t_2$ time delay is scanned by a computerized delay stage which is controlled by home-written LabVIEW programs to characterize the dynamic features of the system. A rotational stage is mounted on the sample stage to choose the tilt angle and, therefore, the wavevector of the driven polaritons. One special requirement for this experiment is that the rotation axis of the stage needs to be parallel to the incidence plane formed by the pump and probe beams. In this way, we ensure that the in-plane wavevectors, $k_{||}$, of pump and probe pulses are the same. The particular $k_{||}$ value the of pump and probe beams are determined by checking the 1D transmission polariton spectra of the pump and probe pulses before and after 2D IR acquisitions.

## Section S1.3. 3D Fourier transformation

2D IR spectra at early times ($t_2$ = 0 ~ 6 ps) show unambiguous oscillating features at the UP (see Fig. 4a) and LP frequencies (see fig. S7a) and their period (0.8 ps) suggests these are Rabi oscillations (~38 $cm^{-1}$). This information provides key evidence of the coherence between the LP and the UP. To obtain the oscillatory part of the total 2D signal, we applied the 3D Fourier transform to the combined 2D matrices at different time delays. An additional frequency axis ($\omega_2$) is generated from applying FFT to the $t_2$ axis. Figures S2a and S2b contains the projections of the 3D FFT of the nonlinear signal into the $\omega_1$-$\omega_2$ and $\omega_3$-$\omega_2$, respectively. These figures clearly show features at $|\omega_2|$ = 38 $cm^{-1}$ (referred to as AC part), in addition to the non-oscillating part at $\omega_2$ ~ 0 $cm^{-1}$ (referred to as DC part). The DC and AC parts can be

disentangled by applying a frequency filter to the 3D matrix followed by an inverse Fourier transform of the DC and AC parts. A representative result is given in Fig. 4b of the main text.

To further analyze the coherent dynamics, amplitudes of the AC part at $\omega_1 = \omega_{UP}/\omega_3 = \omega_{UP}$ and $\omega_1 = \omega_{LP}/\omega_3 = \omega_{UP}$ were extracted and plotted versus $t_2$ (figs. S2c and S2d). The UP-UP oscillating trace exhibits nearly perfect dephasing dynamics and can be fitted with a single exponential giving a lifetime of ~2 ps. Conversely, the LP-UP trace deviates from pure dephasing dynamics, possibly because the overtone transitions of dark reservoir modes ($\upsilon_{12}$ ~ 1968 $cm^{-1}$ and $\upsilon_{23}$ ~ 1950 $cm^{-1}$) perturb the LP state.

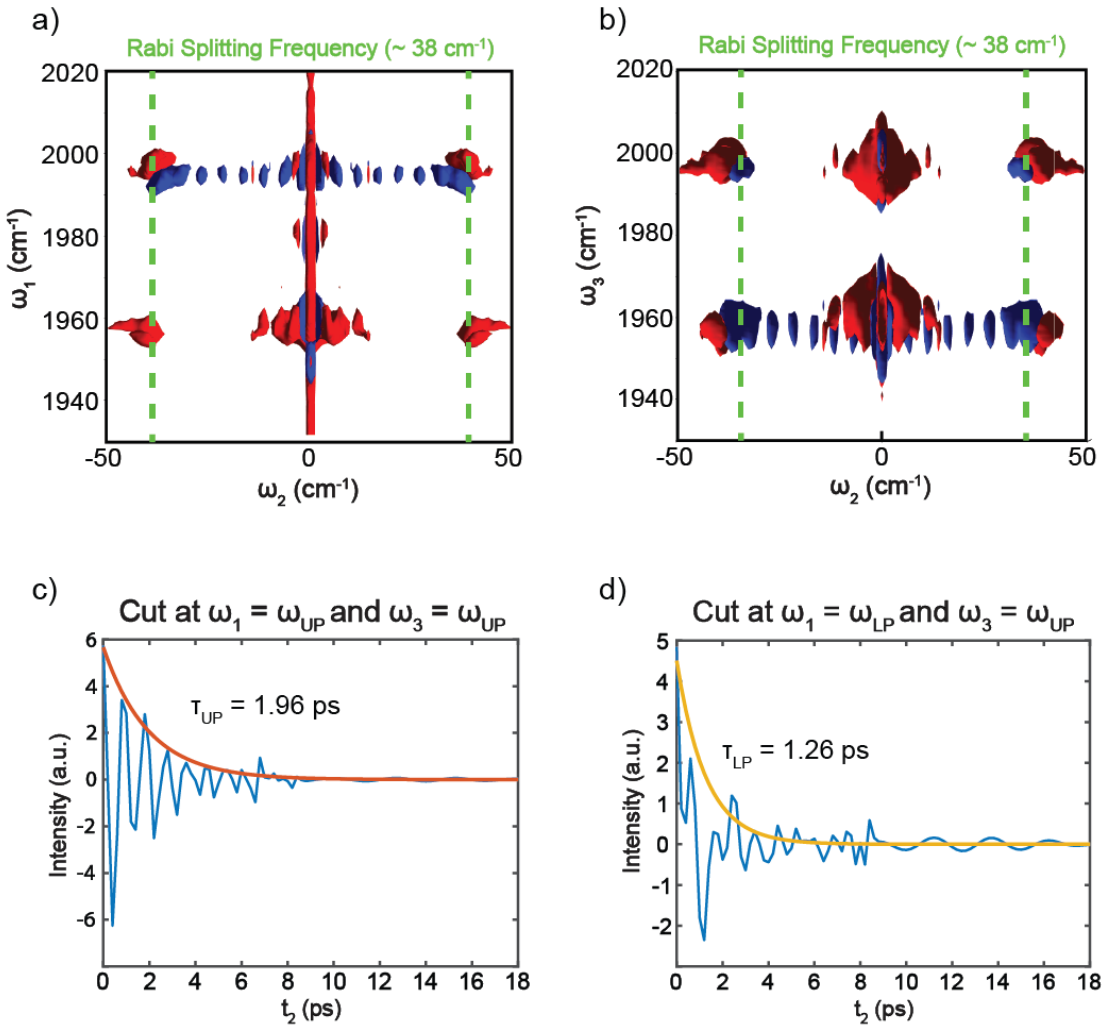


**Fig. S2. 3D FFT frequency domain ($\omega_1$-$\omega_2$-$\omega_3$) spectra.** (a) View from the $\omega_1$-$\omega_2$ plane; (b) View from the $\omega_3$-$\omega_2$ plane; Dephasing traces of (c) cut at $\omega_1 = \omega_{UP}$ and $\omega_3 = \omega_{UP}$, and (d) cut at $\omega_1 = \omega_{LP}$ and $\omega_3 = \omega_{UP}$.

## Section S1.4. Nonlinear signal pump and probe power dependence

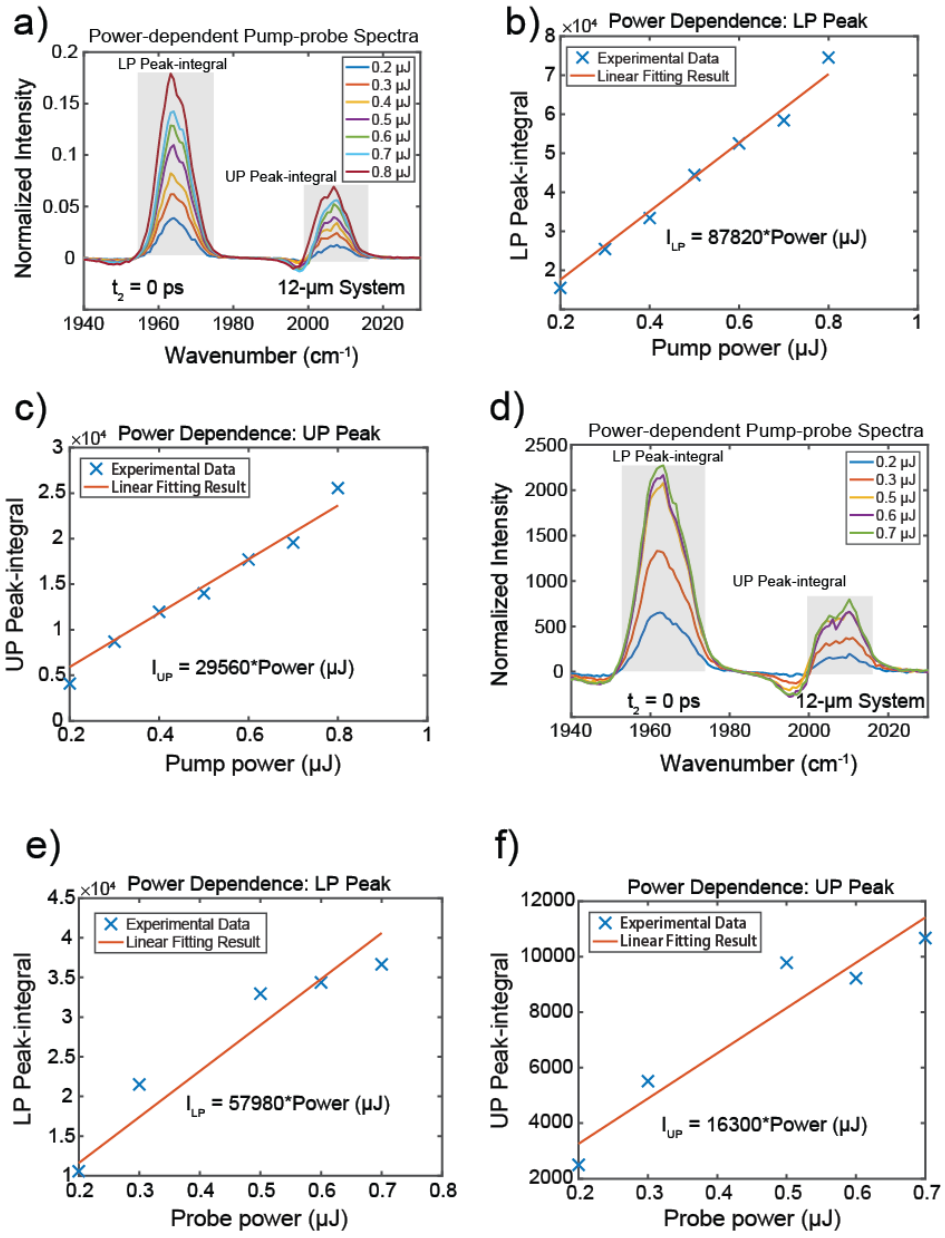


**Fig. S3. IR power dependence.** (a) Pump-probe spectra at $t_2$ = 0 ps for 12-μm polariton system; (b) LP peak integrated signal; (c) UP peak integrated signal. Probe power-dependence: (d) Pump-probe spectra at $t_2$ = 0 ps for 12-μm polariton system; (e) LP peak integrated signal; (f) UP peak integrated signal. Both LP and UP peak integrated signals are proportional to pump/probe power, supported by the fitting equation shown as the insets.

To figure out the scaling of the 'polariton bleach' signal with respect to the pump intensity, we performed a series of power-dependent pump-probe experiments. The self-heterodyned third order signal (ΔT) can be expressed as the equations as follow

$$\Delta T = \left|Sig^{(3)} + Sig^{(1)}\right|^2 - \left|Sig^{(1)}\right|^2 = 2Re\left[Sig^{(3)} * \overline{(Sig^{(1)})}\right] + \left|Sig^{(3)}\right|^2,$$

$$where\ Sig^{(3)} \sim E_{pump}^2 \cdot E_{probe}\ and\ Sig^{(1)} \sim E_{probe}.$$

$$\Longrightarrow \Delta T \propto E_{pump}^2 E_{probe}^2 + O\left(E_{pump}^4 E_{probe}^2\right)$$

Since $(E_{pump})^2$ and $(E_{probe})^2$ are proportional to the pump and probe power, respectively, the signal ($\Delta T$) is proportional to the power of both IR beams whenever higher-order response can be neglected. From the pump-power-dependent results (fig. S3), it is clear that both LP and UP peak integrated signal intensities decrease as pump or probe power reduces. The integrated LP and UP peak intensities are roughly proportional to the pump or probe power (fig. S6b, S6c, S6e and S6f). The linear relations between LP and UP peak-integrals and IR power have been shown as the insets of the corresponding sub-figures.

## Section S2. Supporting results

## Section S2.1. Transmission and transient pump-probe spectra of uncoupled systems

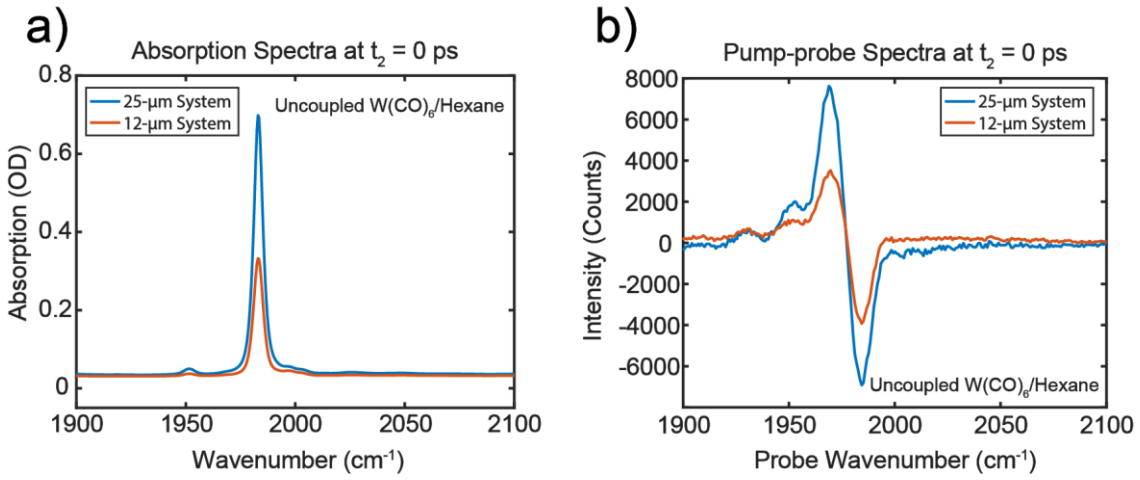


**Fig. S4. Linear transmission and pump-probe spectra of uncoupled $W(CO)_6$/hexane systems with 12- and 25-μm cavity longitudinal lengths.** Results of control experiments for uncoupled $W(CO)_6$/hexane systems with both 12 and 25-micron cell longitudinal lengths at similar concentration: (a) Linear transmission spectra; (b) Pump-probe spectra.

We performed the control experiments with uncoupled $W(CO)_6$/hexane systems with 12 and 25 μm spacers under similar conditions (concentration, IR power, etc). The transmission in fig. S4a shows agreement with Beer's law, the absorption is doubled when the cavity longitudinal length is switched from 12-μm to 25-μm and the ratio between the absorption of 12-μm and 25-μm uncoupled systems is

2.03. In fig. S4b, the pump-probe signal of 25-μm is roughly twice as large as the 12-μm pump-probe signal. Based on the fundamental peak (the only which is negative, around 1983 $cm^{-1}$), the ratio between 25-micron and 12-μm peak intensity is about 2.16, while the 1→2 overtone peak (at roughly probe wavenumber of 1968 $cm^{-1}$) intensity ratio is 1.82. Both ratios are close to 2. Therefore, this result suggests that the 3rd order signal (pump probe) is not enhanced relative to the linear signal (absorption) when the sample length is reduced by a factor of 2.

## Section S2.2. 2D IR and transient pump-probe spectra and 2D-IR spectral cuts

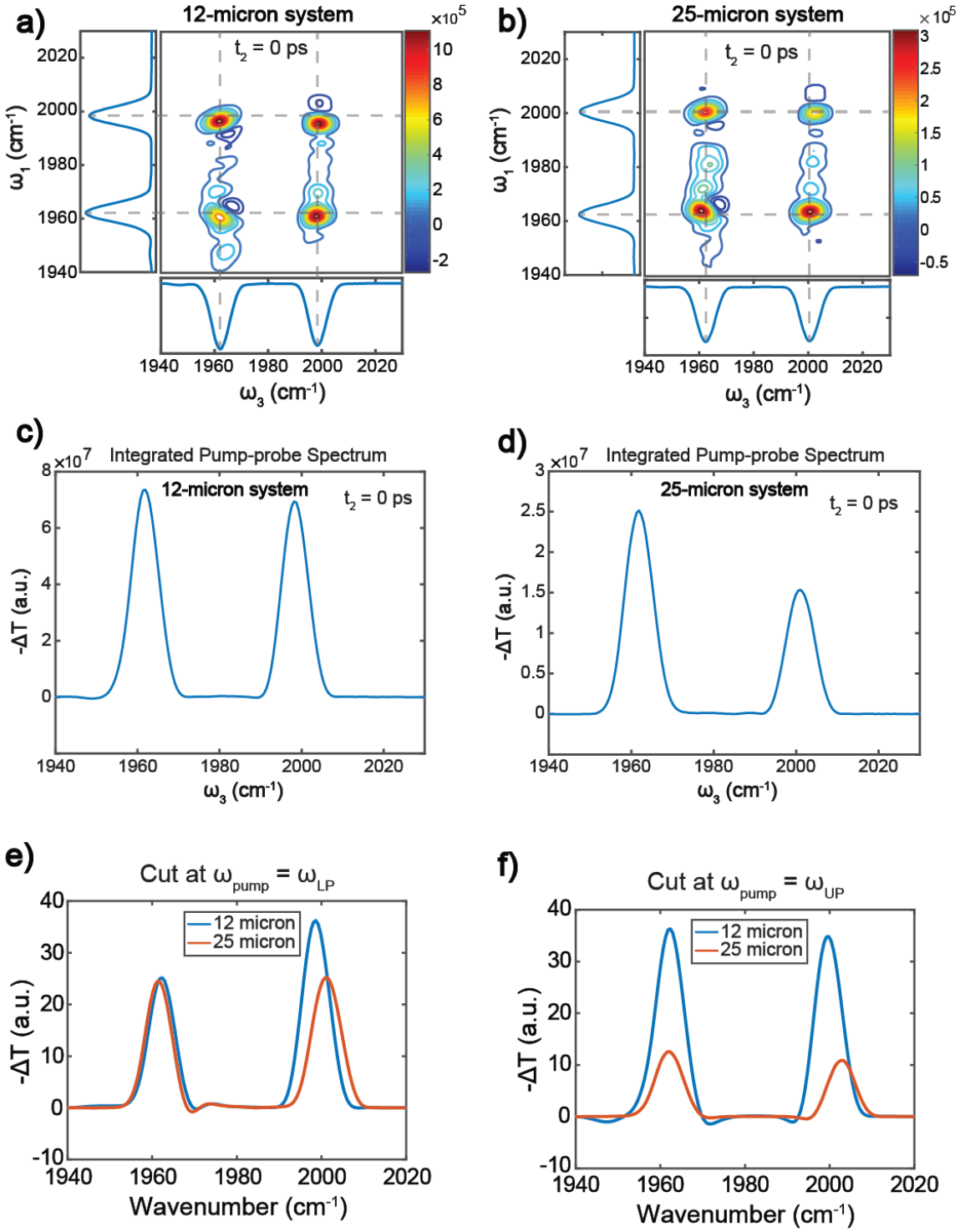


**Fig. S5. Pump-probe and 2D IR spectra and their spectral cuts at LP/UP pump frequencies.** 2D IR spectra of the (a)12 μm and (b) 25 μm systems; Integrated pump-probe spectra of the 12 μm (c) and (d) the 25 μm systems. Note that the color bars of (a) and (b) indicate that 12-micron system has significantly stronger nonlinearities than 25-micron system. 2D IR Spectral cuts of the 12 and 25 μm systems for comparison at (a) $\omega_{pump}=\omega_{LP}$; (b) $\omega_{pump}=\omega_{UP}$. $t_2 = 0$ ps

## Section S2.3. 2D IR spectra for various molecular concentrations

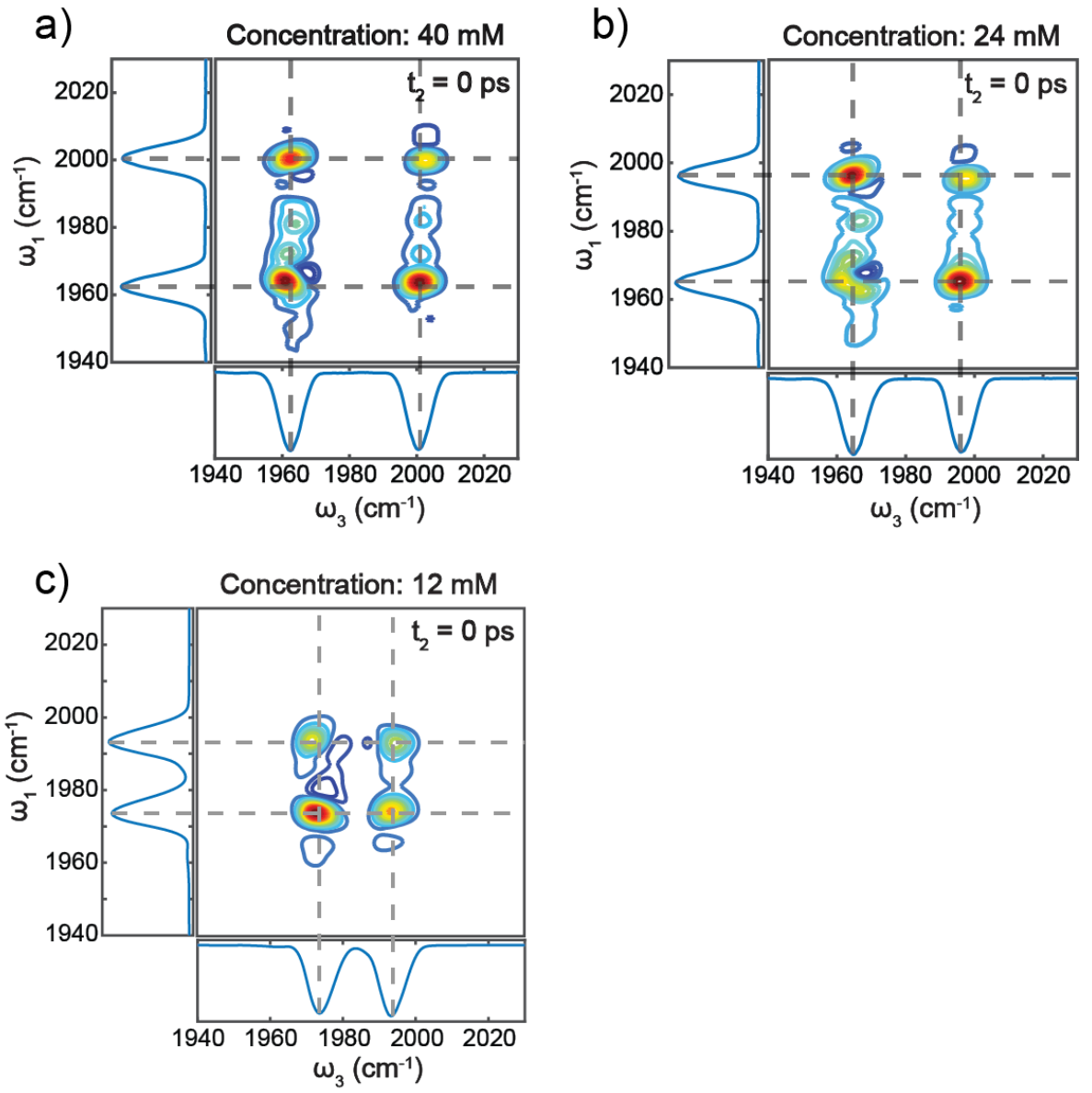


**Fig. S6. 2D IR spectra of the 25-μm system at $t_2$ = 0 ps with various concentrations.** (a) 40 mM; (b) 24 mM;

## Section S2.4. Early-time dynamics of 2D IR spectral cuts

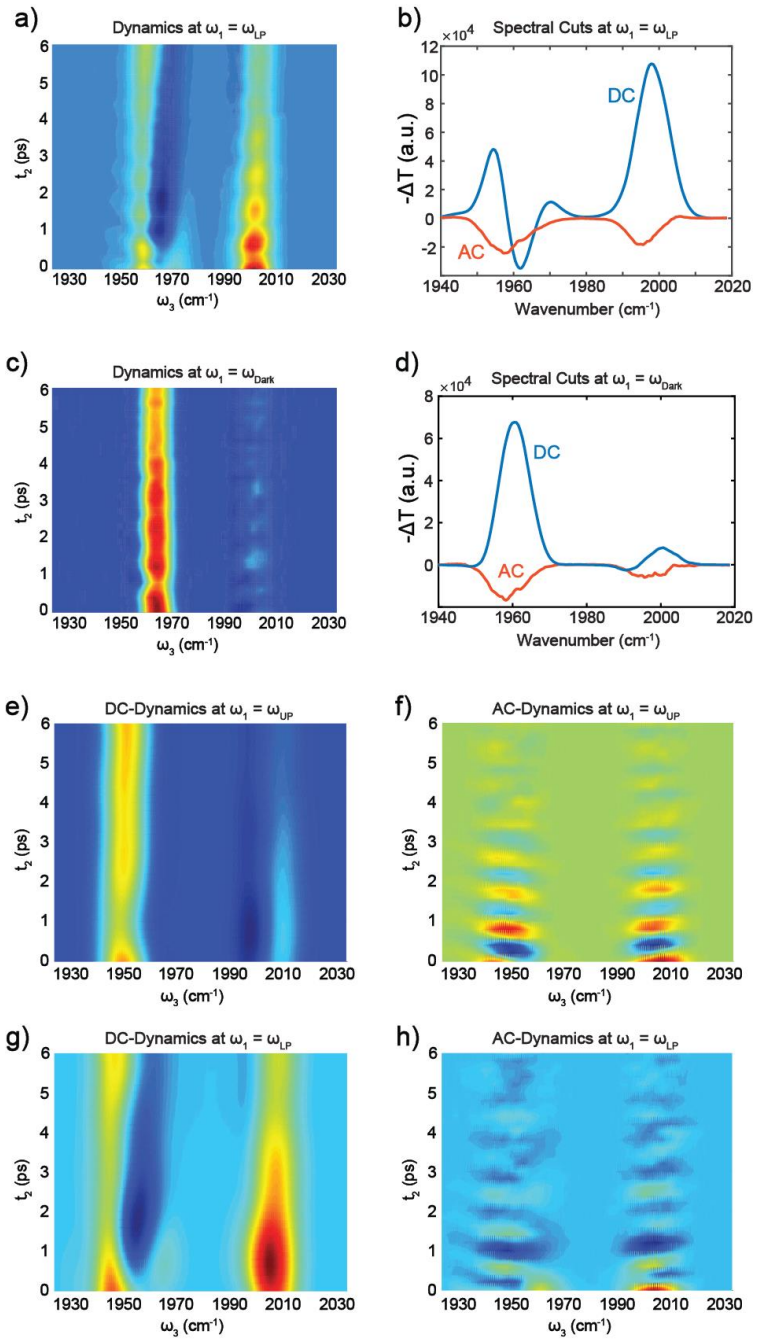


**Fig. S7. Early-time dynamics of 2D IR spectral cuts at $\omega_1 = \omega_{LP}/\omega_{Dark}$ and AC/DC components of LP/UP cuts between 0 and 6 ps.** Early-time dynamics of 2D IR spectral cuts at (a) $\omega_1=\omega_{LP}$ and (c) $\omega_1=\omega_{Dark}$ between -2 to 7 ps. AC and DC differential transmission spectral cuts at (b) $\omega_1=\omega_{LP}$, and (d) $\omega_1=\omega_{Dark}$ at $t_2$=0.8 ps. Dynamics of (e) DC-component at $\omega_1=\omega_{UP}$, (f) AC-component at $\omega_1=\omega_{UP}$, (g) DC-component at $\omega_1=\omega_{LP}$, and (h) AC-component at $\omega_1=\omega_{LP}$.

Figures S7a and S7c show the waiting-time ($t_2$) dynamics of spectral cuts at $\omega_1=\omega_{LP}$ and $\omega_1=\omega_{Dark}$, respectively. We also employed the 3D-FFT (Sec. S1.3) to extract the AC and DC components of each of the mentioned spectral cuts. In figs. S7b and S7d, we show the AC and DC signal contributions to nonlinear signal obtained with $\omega_1=\omega_{LP}$ and $\omega_1=\omega_{Dark}$ at $t_2$ = 0.8 ps, respectively.

Compared to the dynamics of the UP-cut (Fig. 4a), the waiting-time dependent signal measured at the LP-cut (fig. S7a) has significantly stronger integrated DC component, although the oscillatory bleach feature is still obvious (fig. S7b). The relative phase difference between the LP-AC (fig. S7a) and the UP-AC (Fig. 4b) signals is due to the heterodyne detection system which allows us to extract the relative phase between the signals obtained with LP and UP pumping. The enhanced integrated DC signal for an LP-resonant pump is likely a result of the perturbation of the LP by overtone transitions of $W(CO)_6$ dark modes, especially that with $\omega_{12}$ ~ 1968 $cm^{-1}$, which is nearly resonant with the LP ($\omega_{LP}$ = 1964 $cm^{-1}$), and thus perturbs the polariton response even at early-times. When the pump frequency equals that of the bare molecule (dark mode), the oscillatory part of the nonlinear signal is almost negligible (fig. S7c). After Fourier filtering, it does show a very weak AC component (fig. S7d), which may be a result of spectral overlap with the oscillating polariton spectral features. As discussed in the main text and Sec. S3.2, $|UP\rangle\langle LP|$ and $|LP\rangle\langle UP|$ coherence states are required for the observation of Rabi oscillations (AC part). Due to spectral congestion and overlaps, the tail of the AC component of LP and UP peaks can also induce dark mode spectral features to "oscillate" weakly. Nevertheless, as clearly shown in the 3D IR plot (figs. S2a and S2b), the Rabi oscillation peaks near $\omega_2$=38 $cm^{-1}$ only show up at LP and UP transitions, but not at dark mode resonances. This provides strong evidence that dark modes are not involved in Rabi oscillation. In summary, the weakly oscillatory features in the dark mode dynamics, and the stronger contamination of the LP response by dark mode transitions indicate the UP spectral cuts are the most suitable for the analysis of pure vibrational polaritonic response, as performed in the main text.

The early-time dynamics of AC and DC parts of both LP and UP spectral cuts are shown in fig. S7e, f, g and h. The DC parts (fig. S7e and g) of both LP and UP cuts show the expected peak-shifts which evolve continuously. The AC parts (fig. S7f and h), on the other hand, are mostly composed of a convolution of oscillations with dephasing traces (see SI section 1.3 Three-dimensional Fourier Transform for more details). By comparing the DC and AC dynamics, it is clear that the oscillating part which contributes significantly to the 'polariton bleach' signal would dephase within approximately 3 ps, matching with the cavity lifetime. Conversely, the DC parts continue to evolve even after 3 ps. Those dynamic traces further support our statements.

## Section S2.5. Two-component spectral fitting of absorptive pump-probe spectra

In this section, we show that the measured nonlinear signals obtained from the LP and UP (25 μm system) 2D IR spectral cuts at zero waiting-time cannot be reproduced with a simple spectral fitting based on previous studies(*6*, *13*, *14*).

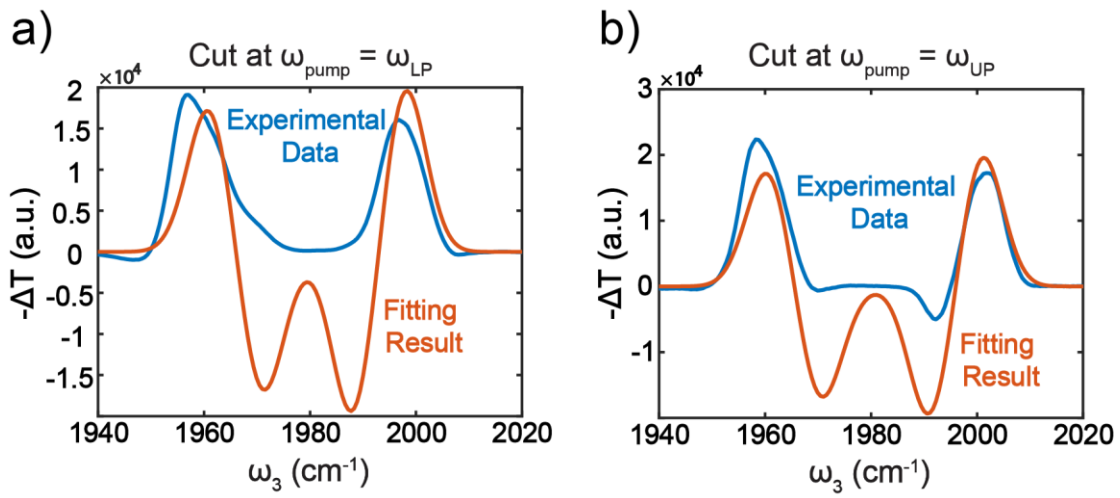


**Fig. S8. Spectral fitting of 25-μm systems with $t_2$ = 0 ps at $\omega_1 = \omega_{LP}$ and $\omega_1 = \omega_{UP}$.** Spectral fitting of 25-μm systems with $t_2$ = 0 ps at (a) $\omega_1=\omega_{LP}$ and (b) $\omega_1=\omega_{UP}$. The fitting model is composed of an absorptive feature on the LP (due to the interference of the LP with dark overtone transitions) and the derivative lineshape at the LP/UP frequencies (due to Rabi splitting contraction). The results indicate that the combined effect of dark mode overtone absorption and Rabi splitting contraction is insufficient to accurately model the experimental features at early times.

A two-component spectral fitting was applied to the LP/UP spectral cuts of 2D-IR spectrum of 25-μm system at $t_2$ = 0 ps, using the following equation

$$Spec_{fit}(x) = \underbrace{\left\{\alpha_1\left[a_0 e^{-\left(\frac{x-b_0}{c_0}\right)^2}\right]\right\}}_{(1)} + \underbrace{\left\{\alpha_2 \sum_{i=1}^{2}\left[a_i e^{-\left(\frac{x-b_i}{c_i}\right)^2} - a_i e^{-\left(\frac{x-b_i+\Delta x}{c_i}\right)^2}\right]\right\}}_{(2)} \quad (1)$$

In this equation, terms (1) and (2) represent spectral components corresponding to dark mode overtone response and the Rabi splitting contraction, respectively. The probed frequency is given by *x*, and *a*, *b* and *c* are the amplitude, resonance frequency and width of a Gaussian peak; Δx is the amount of peak-shift and $\alpha_1$ and $\alpha_2$ are the coefficients which modulate the compositions of the two components.

## Table S1. Parameters of two-component fitting.

| States of Spectral Cuts | Parameters for Gaussian Peaks | | | | | | Compositions | | Polariton Peak-shift ($cm^{-1}$) |
|---|---|---|---|---|---|---|---|---|---|
| | Amplitudes | | Resonance Frequencies ($cm^{-1}$) | | Widths ($cm^{-1}$) | | | | |
| | $a_1$ | $a_2$ | $b_1$ | $b_2$ | $c_1$ | $c_2$ | $\alpha_1$ | $\alpha_2$ | $\Delta x$ |
| **UP** | 17550 | 20000 | 1960.5 | 2001 | 8.1 | 7.7 | 0.1 | 0.5 | 10 |
| **LP** | 17550 | 20000 | 1960.5 | 1998 | 8.1 | 7.7 | 0.1 | 1 | 10 |

From figs. S8a and S8b, it is clear the spectral cuts from the experimental data cannot be fitted with only the two components mentioned in equation (6). Hence, an additional component that represents the polariton-bleach behavior would be needed.

## Section S3. Theory

## Section S3.1. Scaling of polariton nonlinearities

In this section, we show that when the effects of dark modes can be disregarded, the dominant coherent polariton nonlinear interactions induced by quartic couplings (the most relevant interactions at low energies for homogeneous and isotropic systems like the molecular solution studied here) leads to inverse scaling with respect to the cavity longitudinal length *due to polariton delocalization*. We first demonstrate explicitly the inverse dependence with cavity longitudinal length and molecular concentration of vibrational polariton nonlinearities induced by local mechanical and electrical molecular anharmonicity. The discussion is subsequently generalized to include more general types of molecular nonlinearities, including the nonlinear dephasing mechanism which we propose as the source of the polariton bleach effect. The discussion in this section is limited to polariton-polariton interactions relevant at short times relative to their lifetime

Let a planar infrared cavity consisting of two ideal parallel metal mirrors with surface area $S$ separated by longitudinal length $L$ host $N$ molecules homogeneously distributed across the volume $V = SL$. The TE and TM modes of the cavity are obtained by using periodic boundary conditions for the electromagnetic field along the $x$ and $y$ directions and metal-dielectric interface boundary conditions from Maxwell equations. For the sake of simplicity, we retain in what follows only a single TE cavity photon band with modes parametrized by $\mathbf{k} = (k_x,k_y)$ having resonance frequency $\omega(\mathbf{k})$(*43*). The vibrational frequency and position of the molecule $i$ in the set $\{1,...,N\}$ are given by $\omega_i$ and $\mathbf{r}_i = (x_i,y_i,z_i)$, respectively. The light-matter interaction is treated within the dipole approximation in the rotating-wave-approximation (only interactions which conserve the excitation-number are included)(*43*). In the *absence* of anharmonicity, the Hamiltonian of the hybrid system is given by

$$H_0 = \sum_{i=1}^{N} \hbar\omega_i a_i^\dagger a_i + \sum_{\mathbf{k}} \hbar\omega(\mathbf{k}) b^\dagger(\mathbf{k}) b(\mathbf{k}) + \sum_{i=1}^{N}\sum_{\mathbf{k}} \left[\bar{g}_{i\mathbf{k}} a_i^\dagger b(\mathbf{k}) + g_{i\mathbf{k}} b^\dagger(\mathbf{k}) a_i\right] \tag{2}$$

where $a_i$ and $b(\mathbf{k})$ are the molecular and photonic annihilation operators, $g_{i\mathbf{k}}$ is the coupling constant for the interaction between molecule $i$ and cavity mode $\mathbf{k}$ and $\overline{g_{i\mathbf{k}}}$ is its complex conjugate. The detailed form of $g_{i\mathbf{k}}$ can be found elsewhere(*44*). For our purposes, all that is relevant is that

$$g_{i\mathbf{k}} \propto e^{-i\mathbf{k}\cdot\mathbf{r}_i}\sqrt{\omega_{\mathbf{k}}} \tag{3}$$

where $\mathbf{k}\cdot\mathbf{r}_i = (k_x,k_y)\cdot(x_i,y_i)$. Disregarding the inhomogeneous broadening of the molecular vibrations (i.e., supposing all molecular frequencies are equal to $\omega_0$), the polariton modes of this Hamiltonian can be obtained straightforwardly performing a canonical transformation of the local molecular operators into a collective basis adapted to the form of the light-matter interaction given above(*8*). Specifically, the following *bright* molecular operators are defined

$$a(\mathbf{k}) = \sum_{i=1}^{N} \frac{g_{i\mathbf{k}}}{g_{\mathbf{k}}} a_i, \quad g_{\mathbf{k}} = \sqrt{\sum_{i=1}^{N} |g_{i\mathbf{k}}|^2} \propto \sqrt{N} \tag{4}$$

In this model, there exists also $N_d = N - N_k$ dark modes (where $N_k \propto S$ is the total number of cavity photon modes included in the effective description of the electromagnetic modes) which form the complement to the bright operators $a(\mathbf{k})$ in the space of annihilation operators(*8*). In the collective basis, the quadratic part of the Hamiltonian is written as

$$H_0 = \hbar\omega_0 \sum_{\mathbf{k}} a^\dagger(\mathbf{k})a(\mathbf{k}) + \sum_{\mathbf{k}} \hbar\omega(\mathbf{k})b^\dagger(\mathbf{k})b(\mathbf{k}) + \sum_{\mathbf{k}} \left[\bar{g}_{\mathbf{k}} a^\dagger(\mathbf{k})b(\mathbf{k}) + g_{\mathbf{k}} b^\dagger(\mathbf{k})a(\mathbf{k})\right] + \hbar\omega_0 \sum_{d=1}^{N_d} \alpha_d^\dagger \alpha_d \tag{5}$$

where the operators $\alpha_d$ are the annihilation operators of dark modes. The bright normal modes of the above Hamiltonian are given by the lower (LP) and upper polaritons (UP) with annihilation operators written as(*8*)

$$\alpha_{\mathrm{UP}}(\mathbf{k}) = \cos(\theta_{\mathbf{k}}/2)a(\mathbf{k}) + \sin(\theta_{\mathbf{k}}/2)b(\mathbf{k}) \tag{6}$$

$$\alpha_{\mathrm{UP}}(\mathbf{k}) = -\sin(\theta_{\mathbf{k}}/2)a(\mathbf{k}) + \cos(\theta_{\mathbf{k}}/2)b(\mathbf{k}) \tag{7}$$

where the specific form of the mixing angles $\theta_{\mathbf{k}}$ and polariton frequencies $\omega_{\mathrm{LP}}(\mathbf{k})$ and $\omega_{\mathrm{UP}}(\mathbf{k})$ are inessential for our discussion.

In order to describe polariton nonlinearities we introduce molecular anharmonicity to the hybrid cavity Hamiltonian. At low energies (i.e., when only the first few excited-states are probed) only cubic and quartic nonlinearities are relevant(*22*) Retaining only those interactions that preserve the excitation number operator (consisting of the sum of the photonic and phononic number operators) and disregarding nonlocal interactions or interactions with the environment, the nonlinear part of the Hamiltonian can be written generically as[7]

$$H_{\mathrm{I}} = \Delta \sum_{i=1}^{N} a_i^{\dagger} a_i^{\dagger} a_i a_i + \eta \sum_{i\mathbf{k}} \left[ g_{i\mathbf{k}} a_i^{\dagger} a_i^{\dagger} a_i b(\mathbf{k}) + \bar{g}_{i\mathbf{k}} b^{\dagger}(\mathbf{k}) a_i^{\dagger} a_i a_i \right] \tag{8}$$

where $\Delta$ parametrizes the mechanical anharmonicity (deviation from harmonic energy spectrum of a single vibration), $\eta$ quantifies deviations of the *i*th molecule vibrational transition dipole function from linearity with respect to displacement of the molecular mode from its equilibrium position. In the hybrid cavity *normal-mode* basis, $H_{\mathrm{I}}$ can be written as a sum of polariton-polariton, polariton-dark mode, and dark-dark interactions. The polariton-polariton interactions take the following form

$$H_{\mathrm{I}}^{\text{pol-pol}} = \sum_{p_1 p_2 p_3 p_4}^{\mathrm{LP,UP}} \sum_{\mathbf{k}_1 \mathbf{k}_2 \mathbf{k}_3 \mathbf{k}_4} V_{p_1 p_2, p_3 p_4}^{\mathrm{L}}(\mathbf{k}_1, \mathbf{k}_2, \mathbf{k}_3, \mathbf{k}_4) \alpha_{p_1}^{\dagger}(\mathbf{k}_1) \alpha_{p_2}^{\dagger}(\mathbf{k}_2) \alpha_{p_3}(\mathbf{k}_3) \alpha_{p_4}(\mathbf{k}_4) \tag{9}$$

where the $p_i$'s correspond to either LP or UP and $V_{p_1 p_2 p_3 p_4}^{L}(\boldsymbol{k_1}, \boldsymbol{k_2}, \boldsymbol{k_3}, \boldsymbol{k_4})$ are the coupling constants for the corresponding polariton-polariton interactions. The nonlinear coupling arising from mechanical anharmonicity satisfies the following relations

$$\begin{aligned} V_{p_1 p_2, p_3 p_4}^{\Delta}(\mathbf{k}_1, \mathbf{k}_2, \mathbf{k}_3, \mathbf{k}_4) &\propto \Delta \sum_{i=1}^{N} \frac{\bar{g}_{i\mathbf{k}_1}}{g_{\mathbf{k}_1}} \frac{\bar{g}_{i\mathbf{k}_2}}{g_{\mathbf{k}_2}} \frac{g_{i\mathbf{k}_3}}{g_{\mathbf{k}_3}} \frac{g_{i\mathbf{k}_4}}{g_{\mathbf{k}_4}} \\ &\propto \Delta \sum_{i=1}^{N} \frac{e^{-i(\mathbf{k}_1 + \mathbf{k}_2 - \mathbf{k}_3 - \mathbf{k}_4) \cdot \mathbf{r}_i}}{N^2} \\ &\approx c_{\Delta} \frac{\Delta}{N} \delta_{\mathbf{k}_1 + \mathbf{k}_2 - \mathbf{k}_3 - \mathbf{k}_4} \end{aligned} \tag{10}$$

where $\delta_{\mathbf{q}}$ is the discrete delta function and $c_{\Delta}$ is a constant independent of particle number (in the thermodynamic limit). To obtain the last expression we used that the number of molecules is macroscopic, and these are distributed randomly inside the cavity so that the dominant c ontribution to the polariton-polariton interaction preserves the in-plane wave-vector (a similar result would have been obtained if we had assumed the wave-vector is not conserved, but only excitations with *k* close to zero are driven by the pump). For the electrical anharmonicity term we find a similar result

$$V_{p_1 p_2, p_3 p_4}^{\eta}(\mathbf{k}_1, \mathbf{k}_2, \mathbf{k}_3, \mathbf{k}_4) \approx \frac{\eta(\mathbf{k}_1 + \mathbf{k}_2 - \mathbf{k}_3)}{N} \delta_{\mathbf{k}_1 + \mathbf{k}_2 - \mathbf{k}_3 - \mathbf{k}_4} \tag{11}$$

where $\eta(\mathbf{k}_1 + \mathbf{k}_2 - \mathbf{k}_3)$ is a density-dependent coupling constant of the order of the Rabi splitting.

Further simplification arises from noting that the experimental nonlinear response is measured at $\mathbf{k} \approx 0$, and therefore the dominant contributions will have all $\mathbf{k}_i$ close to zero. Taking for simplicity only the (dominant) couplings between polaritons with the same wave-vector, the total nonlinear coupling can be written as as $\sum_{\boldsymbol{k}} F(\boldsymbol{k})/N$, where $F(\boldsymbol{k})$ is independent of particle number. In the continuum limit of the photonic system, it follows that $\sum_{\boldsymbol{k}} F(\boldsymbol{k})/N = (2\pi)^{-2} S \int d\boldsymbol{k}\, F(\boldsymbol{k})/N$. Given that $N = \rho SL$ where $\rho$ is the molecular density, we find that under the discussed assumptions the nonlinear polariton-polariton coupling constant is inversely proportional to $\rho L_z$. It follows that, for a fixed molecular density, increasing the cavity length, leads to an inversely proportional reduction in the dominant nonlinear polariton-polariton interactions. Similarly, for a fixed cavity longitudinal length, an increase in the molecular density reduces the magnitude of nonlinearities of the hybrid microcavity system.

While the results given above derive from the assumed nonlinearities in Eq. (8), they also apply to nonlinear interactions of the vibrational modes with other molecular degrees of freedom (bath modes). In the case of the $W(CO)_6$ solution, the bath contains, in addition to low-frequency intra and intermolecular modes, the carbonyl asymmetric stretch doublet corresponding to the vibrational modes orthogonal to that which interacts with the TE cavity photon. These modes are nearly-degenerate with the dark transitions, and significantly enhance the phase space for the decay of the two-body states $|LP(\boldsymbol{k}), UP(\boldsymbol{k})\rangle$. This process is favored by the fact that the energy of this state is close to twice the energy of the bare fundamental transition when $\boldsymbol{k}$ is such that the cavity photon is resonant with the molecular system. Thus, $|LP(\boldsymbol{k}), UP(\boldsymbol{k})\rangle$ is particularly sensitive to nonlinear dephasing mechanisms. The rate of decay of $|LP(\boldsymbol{k}), UP(\boldsymbol{k})\rangle$ into bath modes via resonant incoherent scattering is also proportional to 1/N as can be seen from the following argument. The perturbative rate of decay is proportional to $\sum_{i=1}^{N} \rho(F) \left|\left\langle F^{(i)} \middle| V_{SB}^{(i)} \middle| LP, UP \right\rangle\right|^2$, where the wave-vector dependence of the polariton states is implicit, $i$ labels each molecule, $V_{SB}^{(i)}$ denotes the interaction between the $i$th molecular vibration and the bath modes, and $F^{(i)}$ labels arbitrary bath states with density $\rho(F)$ which interact only with the $i$th molecule and that have approximately the same energy as the sum of the LP and UP energies. In the molecular basis, this term is proportional to $\sum_{i=1}^{N} \frac{\rho(F)}{N^2} \left|\left\langle F^{(i)} \middle| V_{SB}^{(i)} \middle| 2^{(i)} \right\rangle\right|^2 = \frac{\rho(F)}{N} \left|\left\langle F^{(m)} \middle| V_{SB}^{(m)} \middle| 2^{(m)} \right\rangle\right|^2$, where $m$ refers to an arbitrary molecule, and the last equality was obtained by assuming all molecules have equal matrix elements for their nonlinear interaction with the bath (mean-field approximation). It follows that nonlinear homogeneous dephasing induced by system-bath couplings also lead to the inverse scaling of nonlinearities with respect to the number of molecules, thus verifying the generic character of this polaritonic feature.

We conclude by highlighting that these considerations show that *the inverse scaling with 1/N of the vibrational polariton nonlinear response is fundamentally a consequence of the delocalization of the polariton across the molecular ensembl*e. Therefore, while polariton nonlinearities are intrinsically due to molecular anharmonicity, the electromagnetic coherence fundamentally affects the character of these nonlinearities by allowing them to become extended across the size of the optical cavity, and give the striking size-dependent effects observed by our experiments.

## Section S3.2. Feynman diagrams for the AC signal

In fig. S9, we show the *dominant* Feynman pathways(*22*) (diagrams) that generate the polariton four-wave-mixing (AC) signals (as measured by our experiments) oscillating with the Rabi frequency as a function of delay time $t_2$ (see Sec. S2.4). Each row on the l.h.s of fig. S9 is labeled by a diagonal or cross-peak in the 2D IR spectrum schematically represented on the r.h.s. To each peak in the AC part of the 2D spectrum, there exists two main diagrams associated to probe-induced stimulated emission (SE) and excited-state absorption (ESA). In the SE pathways, the probe pulse stimulates polariton emission, and the final state is the ground $|g\rangle$. On the other hand, ESA induces transitions from polariton states $|LP\rangle$ or $|UP\rangle$ into two-body excitations $|LP, UP\rangle$. The amplitudes of the ESA and SE pathways have opposite sign. In harmonic systems, these amplitudes also have the same intensity, and therefore, there is no nonlinear signal. The nonlinear AC response measured in our experiment is an indication of the lack of cancellation between the ESA and SE pathways represented in fig. S9. Physically, as discussed in the main text, a nonlinear dephasing mechanism operates on the $|LP, UP\rangle$ state which prevents destructive interference between the amplitudes of the SE and ESA pathways, ultimately giving rise to finite nonlinear AC signals which last for $4 - 5$ ps.

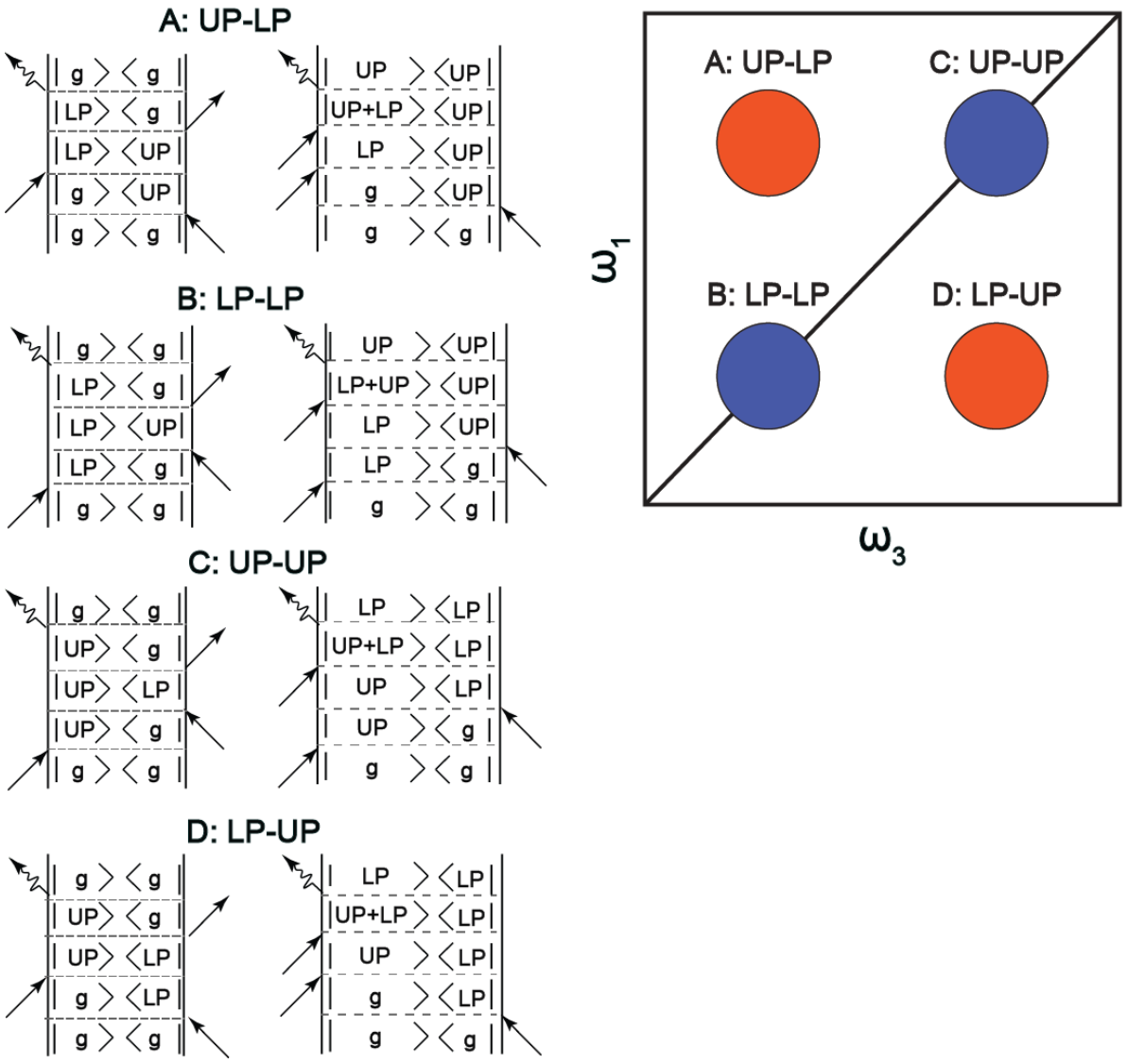


**Fig. S9. Feynman diagrams representing the oscillating nonlinear responses (AC components) in each region.** Feynman diagrams(22) representing the oscillating nonlinear responses (AC components) in each region: A) $\omega_1 = \omega_{UP}$ and $\omega_3 = \omega_{LP}$; B) $\omega_1 = \omega_{LP}$ and $\omega_3 = \omega_{LP}$; C) $\omega_1 = \omega_{UP}$ and $\omega_3 = \omega_{UP}$; D) $\omega_1 = \omega_{LP}$ and $\omega_3 = \omega_{UP}$.

## Section S3.3. Phenomenological simulation of polariton bleach

The classical expression for the steady-state transmission intensity of a Fabry-Perot (FP) cavity containing an isotropic, homogeneous, linear absorptive medium characterized by a frequency-dependent linear susceptibility is given by(*1*, *32*, *45*)

$$T_c(\nu) = \frac{T^2 e^{-\alpha(\nu)L/cos(\theta)}}{1+R^2 e^{-2\alpha(\nu)L/cos(\theta)} - 2Re^{-\alpha(\nu)L/cos(\theta)} cos[4\pi n(\nu)\, cos(\theta)\nu]} \quad (12)$$

where ν is the probed frequency, θ = 0.1 rad is the incidence angle, R = 0.94 and T = 0.06 are the reflectance and transmittance of the employed FP cavity mirrors around the fundamental resonance frequency of the absorptive medium $\nu_1$ =1983 $cm^{-1}$, *L* is the cavity longitudinal length (in the performed simulations, L = 0.00025 cm or 0.000125 cm), *n*(ν) is the real part of the cavity mirror complex refractive index and $\alpha(\nu) = 4\pi j(\nu)\nu$, where j($\nu$) is the imaginary part of the complex refractive index. As mentioned in the main text, by changing the homogeneous linewidth of fundamental mode of $W(CO)_6$, ($\Gamma_1$), the real and imaginary parts of the refractive index *(n, j)* are modulated accordingly (Eqns. (12) − (14)(*1*)). This effect causes variation of the transmission intensity ($T_c$). Specifically, a larger molecular homogeneous linewidth implies enhanced polariton broadening. The oscillator strength of the molecular vibrations is denoted $A_1$. This quantity is proportional to the density of molecular absorbers. Adjusting $A_1$ does *not* lead to the purely absorptive polariton bleach feature, instead, it causes polariton resonance shifts in frequency, i.e. Rabi splitting contraction. Thus, the semiclassical simulation results indicate that changes of $\Gamma_1$, but not $A_1$, cause polariton bleach features. The following are the quantities which are required for the computation of the transmission with Eq. (12)

$$n(\nu) = \sqrt{\frac{\varepsilon_1 + \sqrt{\varepsilon_1^2 + \varepsilon_2^2}}{2}}\ ,\ \ j(\nu) = \sqrt{\frac{-\varepsilon_1 + \sqrt{\varepsilon_1^2 + \varepsilon_2^2}}{2}} \tag{13}$$

where $\varepsilon_1$ and $\varepsilon_2$ are the real and imaginary parts of dielectric constant, expressed as

$$\varepsilon_1 = \varepsilon_{inf} + \sum_{i=1}^{2}\left[\frac{A_i(\nu_i^2 - \nu^2)}{(\nu_i^2 - \nu^2)^2 + (\Gamma_i\nu)^2}\right],\quad \varepsilon_2 = \sum_{i=1}^{2}\left[\frac{A_i\Gamma_i\nu}{(\nu_i^2 - \nu^2)^2 + (\Gamma_i\nu)^2}\right] \tag{14}$$

where we set the background dielectric constant at infinite frequency to be $\varepsilon_{inf}$ = 2.0135, $\nu_i$ are the frequencies of the $0 \rightarrow 1$ and $1 \rightarrow 2$ asymmetric stretch transitions of $W(CO)_6$ given by $\nu_1$ = 1983 $cm^{-1}$, and $\nu_2$ = 1968 $cm^{-1}$, and the $\Gamma_i$ are the linewidths of the corresponding vibrational modes ($\Gamma_1$ and $\Gamma_2$ are 3.0 and 4.5 $cm^{-1}$, respectively). The oscillator strength $A_1$ = 3200 $cm^{-1}$ is chosen so the linear transmission resonance frequencies match the experimentally observed with incidence angle θ = 0.0873 rad, while $A_2$ is neglected, since the fundamental mode has the largest population and is in resonance with the cavity photon.

## Section S3.4. Cavity coherence volume

We estimate the coherence volume of the optical cavity by using the following equation(*46*)

$$V_{\text{eff}} = S_{\text{eff}} \cdot l = \frac{\pi l^2 \lambda_\nu}{1 - R} \tag{15}$$

where $V_{\text{eff}}$ and $S_{\text{eff}}$ are the effective volume and area of a specific cavity mode, $l$ is the cavity longitudinal length (12 and 25 μm), $\lambda_v$ is the wavelength of vibrational transition (5042.86 nm in our case, corresponding to 1983 $cm^{-1}$) and $R$ is the reflectivity of the DBRs which is 96% in the experiments.

Using Eq. (7), we find the coherence volumes of the 12 and 25 μm systems are $0.57\times10^5$ and $2.5\times10^5 \mu m^3$, respectively, i.e., the cavity with longest length has a coherence volume that is approximately four times greater than that with the shortest.